Human Red Blood Cell Properties and Sedimentation Rate: A Biomechanical Study

Natalya Kizilova[1(✉)], Liliya Batyuk[2], and Vitalina Baranets[3]

[1] Warsaw University of Technology,
Nowowiejska street, 24, 00-665 Warsaw, Poland
n.kizilova@gmail.com
[2] Kharkov National Medical University,
Nauki avenue, 2, Kharkiv 61022, Ukraine
[3] Kharkov National University, Svobody square, 4, Kharkiv 61022, Ukraine

Abstract. Human blood is widely used for clinical diagnostics due to its easy accessibility and high sensitivity for any metabolic disorders and diseases. In the paper different mechanical and electric properties of red blood cells (RBC) useful for diagnostics are discussed. The experimental data on the erythrocyte sedimentation rate (ESR) test in its standard procedure and continuous computer assisted assessment are presented. The review of mathematical approaches for reasonable ESR estimation is given. The continuous model of blood as three phase suspension is used for numerical estimation of aggregate ability of RBC. The problem on RBC aggregation and sedimentation in a thin vertical tube is considered. A numerical solution of the formulated hyperbolic problem is obtained by the method of characteristics. Numerical computations have been carried out for a wide range of RBC parameters proper to healthy state and patients with cancer, drug and food allergy. It is shown the continuous sedimentation curves give more diagnostic information than the standard ESR value. Based on the experimental and theoretical study, a biomechanical interpretation of the ESR curves is proposed.

Keywords: Biomechanics · Erythrocyte sedimentation rate
Medical diagnostics

1 Introduction

Blood is a unique tissue circulating between all the cells, tissues and organs of the body and carrying the organic and mineral components as well as products of the tissue metabolism, new growth, cellular apoptosis, and other physiological processes [1]. In that way, blood is the most proper tissue for easy and detailed diagnosis of the body metabolism and state [2]. Any sort of ionic, osmotic or other disease-related changes produce noticeable variations of the membrane surface properties of the red blood cells (RBC) that compose ~40–49% of the blood volume [1, 2]. Therefore, the electric (electric surface charge, electric conductivity, dielectric permittivity), mechanical (density, membrane shape, thickness, deformability, fluidity) and other physical

K. Arkusz et al. (Eds.): BIOMECHANICS 2018, AISC 831, pp. 3–22, 2019.
https://doi.org/10.1007/978-3-319-97286-2_1

(adhesiveness) properties of RBC can be used for early diagnostics of pathological processes [2]. One of the most common and easy clinical tests is the erythrocyte sedimentation rate (ESR) test. The ESR value is the height of the clean blood plasma (BP) zone formed over the RBC zone during gravitational sedimentation of RBC in the blood sample placed into a thin vertical tube. There are several distinct test methodology (Wintrobe, Westergren, Panchenkov) with different blood type (arterial or venous), length (10–30 cm) and diameter (1–4 mm) of the tube, and duration of the test (1–3 h) accepted in different countries [2, 3]. The ESR is an excellent index of inflammatory state associated with cancers, infections, and autoimmune diseases like systemic vasculitis, temporal arteritis, polymyalgia rheumatica, and others. Inflammations cause abnormal proteins to appear in blood and change the surface properties of RBC that promotes their aggregation and faster sedimentation [4–6]. Disregarding the long history of the ESR test [7] and its numerous modifications [2], recently published reviews and research papers on novel aspects of anomalous high [8, 9] and low [10] ESR, its applicability to the elderly [9] and young [11] patients, as well as in pregnancy [12] revealed new approaches for the test procedures and data analyses. During the last decades novel approaches for ESR-based diagnosis of hypercholesterolemia [13], heart failure [14], osteomyelitis [15], and other specific diseases have been proposed.

In this paper a short comprehensive review on the RBC physical properties and aggregation ability, and on mathematical models for EBS modelling and computation of the ESR (normal, pathologically fast or short) is given. The results of measurements of ESR in healthy volunteers and patients with drag and food allergy are presented.

1.1 Electric and Mechanical Properties of RBC

Blood as a concentrated suspension of red blood cells (RBC) is characterized by passive electric properties like electric impedance, conductivity, and dielectric permittivity. Electromechanical properties of BP and blood cells (erythrocytes, leucocytes and platelets) determine RBC and platelets interaction and aggregation, blood rheology and blood clot formation, blood flow through the vessels and tubes of biomedical units [1, 2, 16]. Passive electric property is electric resistivity $\mathrm{Z} = \delta\phi/\mathrm{I}$ that is the ratio of the applied electric potential $\delta\phi$ to the electric current I measured in the sample. Electric resistivity of biological tissues depends on water contents, ionic strength of BP, membrane conductivity and some other biophysical factors. When a constant electric potential $\delta\phi$ is applied to a tissue, the electric current I through it decreases due to generation a counter directed electromotive force E, and the Ohm's law is $\mathrm{Z} = (\delta\phi - \mathrm{E})/\mathrm{I}$. To avoid the electromotive force induction, the measurements are usually conducted in oscillating electromagnetic fields (EMF), and the complex impedance $\tilde{\mathrm{Z}} = \mathrm{Z} + \mathrm{iX}$, where X is the reactance is measured. The values Z, X for different tissues in healthy state and at different diseases have been measured and classified in biophysical handbooks [2].

The biological tissues are not ideal dielectrics and their dielectric properties are described by complex dielectric permittivity $\varepsilon^* = \varepsilon + \mathrm{i}\varepsilon'$, where ε is the real permittivity, $\varepsilon' = \sigma/(2\pi\mathrm{f})$, $\sigma = \mathrm{Z}^{-1}$ is electric conductivity, f is the EMF frequency. The ratio

$\alpha_\varepsilon = \text{atan}(\varepsilon'/\varepsilon)$ determines the tangent of dielectric loss due to transfer of some EMF energy into heat and dielectric relaxation [16, 17].

RBC and other cells in aqueous conditions at physiological pH values have negative electric surface charge $\sigma_e = q/S$, where q is the charge of the cell, S is its surface area, produced by dissociation of the membrane proteins, ion absorption and water hydration layers formed at the cellular surfaces [16]. The surface charge of healthy RBC was found within the limits $\sigma_e = 3 \cdot 10^{-3} \div 1.5 \cdot 10^{-2}$ S/m^2. The surface charge can be quantitatively estimated by electrophoretic mobility (EPM) of the cells in external static electric field, which is the ratio of the cell velocity to the strength of the applied field. Healthy RBC demonstrate EPM = 1.1 – 1.3 μm/s/V/cm [16].

The dielectric permittivity of native blood [17, 18] and RBC suspensions [19, 20] have been thoroughly examined for the medical diagnostic purposes. In the external EMF electric and dielectric properties of biological tissues demonstrate dispersion, i.e. dependence of ε and σ on the EMF frequency f: α – dispersion at low frequencies (f = 10 – 10^3 Hz), β – dispersion in the radio wave range (f = 10^4 – 10^8 Hz), and γ – dispersion in the microwave range (f > 10^{10} Hz). In the native blood and RBC suspensions α – dispersion is almost absent; β – dispersion is determined by noticeable decrease in capacity of the cell membranes, and dipole polarization of hemoglobin, membrane and BP proteins; and γ – dispersion is determined by polarization of water molecules, and structure and behavior of the hydration shells of RBC [13, 14]. The ε and σ values for native human blood at low and high frequency limits are ε = 7350, σ = 0.49 S/m and ε = 160, σ = 0.9 S/m accordingly [17].

Mechanical properties of RBC (size, shape, deformability, viscoelasticity) are related to their electrical characteristics. Inside the organism blood moves through the blood vessels at a strong influence of electric fields generated by contracting heart, skeletal and smooth muscles, and therefore the electric properties of RBC and BP influence their movement, blood viscosity, and efficiency of the transport of oxygen, carbon dioxide, mineral, organic and other components. Blood viscosity as a main determinant in hemodynamics, depends on RBC concentration, size, shape and deformability, protein concentration in BP, temperature, and shear rate in the flow [1, 16]. In the inflammation state, cancer, necrosis and other severe diseases the fragments of membranes, specific proteins and viruses can modify the RBC membranes, change their hydration shells [20], decrease their surface charge [16] and, therefore, increase their aggregate ability that leads to high ESR [3–6, 8, 9]. When the RBC membranes are overloaded by absorbed particles and cations, cholesterol or other substances their charge is decreased and their membrane become thicker that essentially increases RBC rigidity and decreases their deformability and ability to pass through the capillaries [1, 2].

The most relevant quantitative estimations of the RBC electromechanical properties and aggregate ability for medical diagnostics purposes can be carried out by EPM based estimations of the electric charge [2, 16], microwave dielectric spectroscopy [17–20], and ESR tests [1, 2].

1.2 RBC Aggregation in Health and Pathology

Healthy RBCs demonstrate reversible rouleaux formation, i.e. elongated aggregates composed by chains of RBC stacked together as coins. The aggregates are easily

destroyed by shear stress in the blood flow through the vessels or tubes of the external blood circulation/oxygenation systems. In the slow flows and in the stagnant regions of secondary flows the RBC can form more complex aggregates of >100 cells, thus, hampering the circulation and increasing the RBC sedimentation, because larger aggregates settle faster in the gravity field.

Microscopic methods for estimation of RBC aggregation rate are based on direct counting of the average number of cells in the chains on the dry smears (smeared drop of blood deposited on a glass slide) or on micro images of diluted blood [21, 22]. Optical methods based on light scattering patterns in the colloidal systems and suspensions are also used for the RBC aggregation rate estimation [21, 23].

According to electron microscope images, there are narrow gaps between the flattened sides of RBC, and the width of the gap corresponds to the length of a bridge molecule, which is fibrin in normal blood, and other polymer molecule at experimental conditions (polylysine, dextrans, etc.) [21]. The bigger number of bridges provides stronger binding of RBC in the aggregates. Adhesions of the bridge molecules at RBC surfaces are reversible and can be destroyed by shear stresses and chemical influences [22]. At physiological pH when RBC have negative surface charge and the bridge molecules have positive charged ends, aggregation is determined by the electrostatic forces, while for neutral or negatively charges ends it is determined by van-der-Vaals forces and hydrogen binds which are less stable for deformations. In that way, the microphysical theories of RBC aggregation are based on physics of double electric layers and hydrate shells, electric and viscoelastic interactions of cellular surfaces and bridge molecules [23, 24].

The Monte-Carlo simulations of geometry and fractal properties of the aggregates composed by absorption of particles with determined electric potentials revealed that aggregation is a very complex phenomena even in binary mixtures and needs additional experimental and theoretical studies [25]. RBC aggregation is much more complex process that is influenced by pH of blood, cell shape, electric and adhesive properties, and deformability. Different medicines and toxins produced by microorganisms and viruses cause various changes in the mechanical and electric properties of RBC and BP. The simplest microphysical model of RBC aggregation is based on Newton dynamic law [26]

$$m_i \frac{d\bar{v}_i}{dt} = \sum_{i \neq j} \bar{f}_{ij} + \bar{f}_i^h, \tag{1}$$

where m_i is the mass of i-th particle, $\bar{v}_i$ is its velocity, $\bar{f}_{ij}$ is the force acting on i-th particle from j-th particle, $\bar{f}_i^h$ is the hydrodynamic force.

Generally speaking, the forces $\bar{f}_{ij}$ could be divided into attraction forces $\bar{f}_{ij}^a$ promoting particle approaching, interaction and binding, and repulsive forces $\bar{f}_{ij}^r$. One of the repulsive forces is the elastic repulsion $\bar{f}_{ij}^e$ determined by physical occupation of space by the contacting particles, their elastic deformation and interaction as viscoelastic fluid-filled charged shells. Then $\bar{f}_{ij} = \bar{f}_{ij}^a + \bar{f}_{ij}^e$ where

$$\bar{f}_{ij}^{e} = \begin{cases} k\left(r_i + r_j - d_{ij}\right)^{3/2}\bar{n}_{ij} & \text{if } d_{ij} \le r_i + r_j \\ 0 & d_{ij} > r_i + r_j \end{cases}, \tag{2}$$

where $r_{i,j}$ are radiuses of the i-th and j-th particles interacting, d_{ij} is the distance between their physical centers, $\bar{n}_{ij}$ is the unit vector directed from j-th to i-th particle.

Interaction of two particles depends on their Morse potentials

$$\Phi_{ij} = D_{ij}\left(e^{2B\left(\delta_0 - \delta_{ij}\right)} - 2e^{B\left(\delta_0 - \delta_{ij}\right)}\right),$$

where D_{ij} are the coefficients describing surface properties, $\delta_{ij} = \left(d_{ij} - r_i - r_j\right)$ are the distances between the surfaces of the interacting particles, $\delta = \delta_0$ if $d_{ij} < r_i + r_j$, B is the scalar coefficient which is inverse to the double electric layer thickness.

Then the attraction force can be written as

$$\vec{f}_{ij}^{a} = -\frac{\partial \Phi_{ij}}{\partial \delta_{ij}} A = 2D_{ij}AB\left(e^{2B\left(\delta_0 - \delta_{ij}\right)} - e^{B\left(\delta_0 - \delta_{ij}\right)}\right)\vec{n}_{ij}, \tag{3}$$

where A is the area of the contact surface of the particles.

The values B, δ_0, D_{ij} can be taken as computed for ideal charged surfaces and corrected then according to experimental data. Hydrodynamic force is usually estimated from the Stokes law for rigid particle and slow flow at low Reynolds numbers

$$\vec{f}_i^{h} = k\mu r_i(\vec{v}_i - \vec{v}_\infty), \tag{4}$$

where μ is the fluid viscosity, $\vec{v}_i$ and $\vec{v}_\infty$ are the velocities of the particle and undisturbed flow, k is the shape coefficient that is $k = 6\pi$ for a sphere.

For the concentrated suspensions (C > 5%) $\mu = \mu(C, \dot{\gamma})$, where C is the concentration of particles, $\dot{\gamma}$ is the flow shear rate. More detailed models account for non-steady flow, inertia, Magnus effect, and the following expression can be used instead of (10) [24]:

$$\begin{aligned} \vec{f}_i^{h} &= k\mu r_i(\vec{v}_i - \vec{v}_\infty) + k_1\mu\Delta\vec{v}_\infty - k_2\rho r_i^3\frac{d}{dt}(\vec{v}_i - \vec{v}_\infty) \\ &+ k_3\rho r_i^3(\vec{\omega}_i - \vec{\omega}_\infty) \times (\vec{v}_i - \vec{v}_\infty) + k_4\sqrt{\mu\rho}r_i^2\int\limits_{-\infty}^{t}\frac{d}{d\tau}(\vec{v}_i - \vec{v}_\infty)\frac{d\tau}{\sqrt{t-\tau}}, \end{aligned} \tag{5}$$

where $\vec{\omega}_i$ and $\vec{\omega}_\infty$ are angular velocities of the i-th particle and fluid, k_{1-4} are particle specific coefficients.

Numerical computations on the model (1)–(5) revealed significant variations in the RBC aggregation rate produced by particle shape coefficient, concentration, electric charge and rigidity [24]. The presented microrheological model of RBC movement, interaction and aggregation will be used in the next chapters for the continual modeling of blood as a multiphase fluid.

1.3 Continuous Modeling of RBC Aggregation and Sedimentation

In the continual mechanics approach the blood is considered as a multiphase suspension of free RBC (1) and RBC aggregates (2) suspended in the BP (3). During the aggregation and disaggregation the solid phases exchange their mass, momentum and energy when free RBC pass on from the phase 1 into phase 3 and vice versa. Mass, momentum and energy balance equations can be obtained from thermodynamics of the multiphase continua. The BP is usually modeled as an incompressible Newtonian liquid [27, 28]. In the single phase approach the mass and momentum balance equations have the simplest form

$$\mathrm{div}(\vec{\mathrm{v}}) = 0, \rho \frac{\mathrm{d}\vec{\mathrm{v}}}{\mathrm{dt}} = -\nabla \mathrm{p} + \mathrm{div}(2\mu\hat{\mathrm{e}}), \tag{6}$$

and must be completed by the equation of aggregation kinetics

$$\frac{\mathrm{dN}}{\mathrm{dt}} = \Gamma^{+}(\mathrm{N}, \mathrm{I_e}) - \Gamma^{-}(\mathrm{N}, \mathrm{I_e}), \tag{7}$$

where N is the number of aggregates per unit volume, $\vec{\mathrm{v}}$ is the velocity, p is the hydrostatic pressure, $\hat{\mathrm{e}}$ is the strain rate tensor, $\mathrm{I_e}$ is the second invariant of $\hat{\mathrm{e}}$, ρ is density, $\mu = \mu(\mathrm{I_e})$ is the dynamic viscosity, $\Gamma^{\pm}$ are the aggregation and disaggregation rates accounting for different physical mechanisms (4).

Expression for Γ can be reconstructed from the microrheological theory (1)–(5) or by dimension analysis. For instance, a good approximation for the quasi-steady pulsatile flow of thixotropic liquid in the cylindrical tube can be obtained by assuming [27, 28]

$$\Gamma = -\alpha^{+}\mathrm{I_e}\mathrm{N_0}\mathrm{n}^{1-\gamma^{+}} + \alpha^{-}\mathrm{I_e}\mathrm{N_0}\mathrm{n}^{1-\gamma^{-}}(1-\mathrm{n})\chi(1-\mathrm{n})\mathrm{f}\left(\frac{2\mu\mathrm{I_e}}{\sigma*}\right), \tag{8}$$

where $\mathrm{n} = \mathrm{N}/\mathrm{N_0}$ is the dimensionless numerical concentration of the aggregates, $\mathrm{N_0}$ is their initial concentration, $\alpha^{\pm} = \mathrm{const} > 0$, $\gamma^{\pm}$ are shape coefficients ($\gamma^{\pm} = 0$ for spherical particles), $\sigma*$ is the critical stress destroying the aggregates, χ is the Heviside function, f is a monotonous non-decreasing dimensionless function.

Different types of flows of thixotropic suspensions of aggregating particles in tubes and channels, flow stability and aggregation stability have been studied based on the model (6)–(8) [28, 29].

The more detailed model accounting for liquid capture inside the aggregates followed by its progressive squeezing out from the aggregates, i.e. the exchange between the phases 2 and 3, has been developed in [27]. The model is based on the mass and momentum balance Eq. (6), while the following balance equations for numerical (N), mass (C) and volumetric (H) concentrations of the aggregates are accepted instead of (8)

$$\frac{\mathrm{dN}}{\mathrm{dt}} = -\mathrm{div}\,\vec{\mathrm{J}}_{\mathrm{N}} + \Gamma_{\mathrm{N}}, \frac{\mathrm{dH}}{\mathrm{dt}} = -\mathrm{div}\,\vec{\mathrm{J}}_{\mathrm{H}} + \Gamma_{\mathrm{H}}, \frac{\mathrm{dC}}{\mathrm{dt}} = -\mathrm{div}\,\vec{\mathrm{J}}_{\mathrm{C}}, \tag{9}$$

where Γ_{H} is the BP capture inside the aggregates, $\vec{\mathrm{J}}_{\mathrm{N,H,C}}$ are the corresponding diffusion fluxes; according to reversible thermodynamic approach they are linear functions of the corresponding thermodynamic forces, namely

$$\vec{J}_H = -D_{HH}\nabla H - D_{HC}\nabla C - \frac{D_{HN}}{N}\nabla N - \frac{D_{HI}}{I_e}\nabla I_e. \quad (10)$$

Some simplified problem formulations based on (6), (9), (10) and analysis of the model parameters were given in [28, 30, 31].

2 Materials and Methods

The experimental study has been carried out in the Allergy Lab of Kharkov Institute of Dermatology (Ukraine). The native venous blood samples were collected from 20 patients (10 males and 10 females; average age 59 ± 9 years) and split into small portions V = 1 ml. One portion was studied as a control test while into other portions small amounts of the drugs prescribed to the patient by his/her doctor were added. All the portions have been placed in the standard glass tubes (d = 1 mm, L = 100 mm) and microtubes (d = 0.5 mm, L = 50 mm). The tubes were placed in a rack in a vertical position for 3 h at the room temperature. The height h of the transparent layer of blood plasma in the upper part of each tube has been measured each 10 min. As a result of the study the sedimentation curves h(t) have been obtained for each tube. The standard ESR value was computed at t = 1 h of sedimentation.

The curves have been smoothed by a Bayesian filter and the time derivative curves $h'(t)$ have been computed. The typical results of the simultaneous ESR test for the blood of the same patient in the standard tubes and the microtubes are presented in Fig. 1. Thick solid lines in Fig. 1a–d correspond to the control sample and the ESR <10 mm indexes correspond to healthy individuals [2]. The addition of the potential allergen influences on the sedimentation rate by some acceleration or deceleration of the ESR process. Since ESR is determined by the aggregate ability of the RBC in the sample, that means a direct influence on the allergen on the RBC surface. The cases with no allergy for the added drugs are presented in Fig. 1a–d by thin solid lines, while the cases with the confirmed allergy denoted by dashed lines.

The curves $h'(t)$ exhibit similar dynamics (Fig. 1b) with the noticeable maximum at $t = t_{max}$, which corresponds to the maximal velocity of sedimentation followed then by some decrease in the ESR. The decrease in the ESR is caused by the influence of the settled aggregates accumulated at the bottom of the sedimentation tube [33]. The time t_{max} was shown to be a good diagnostic index, which almost independent on the initial concentration of RBC and BP viscosity, and reflects the RBC aggregation rate only [24].

When ESR test is carried out in a microcapillary, a smaller amount of blood is needed and the behavior of the ESR curves in the standard (Fig. 1a) and micro (Fig. 1c) tubes is similar. The difference between the control sample and the sample affected by potential allergens were more distinct in the microtubes (Fig. 1c). The maximal velocity was reached in the microtubes well earlier (t = 35 min) and the dispersion was more noticeable. The peaks in the $h'(t)$ curves in the microcapillary are more acute, i.e. the corresponding time intervals are shorter that allows more precise ESR estimation from the curves. The secondary peaks in ESR at t = 80 min have been detected in the microcapillaries only (Fig. 1d). In that way, when t_{max} is used as a

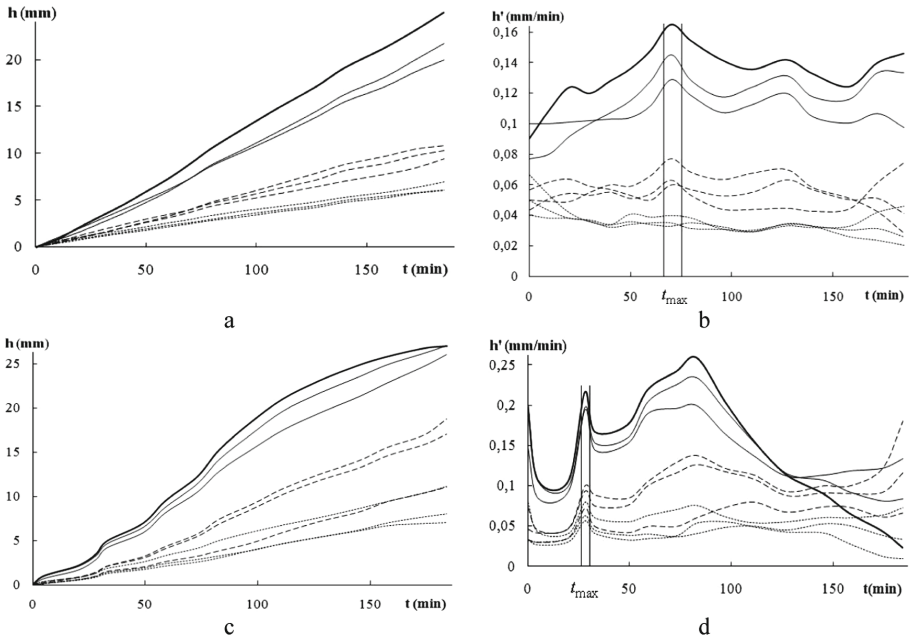

Fig. 1. Experimental curves h(t) (a, c) and h′(t) (b,d) in the standard tubes (a, b) and the microtubes (c, d); solid lines correspond to the control, dashed and dotted lines – to two different potential allergens (medicines).

diagnostic index instead of ESR, the test in the microtubes gives the results earlier, in 30–40 min of the sedimentation process. Thus, the diagnostic information here can be obtained faster, more accurate, and by using a smaller portion of the blood when the microtubes are used.

The results of 20 simultaneous ESR tests with the blood of the same patient conducted in the microtubes are presented in Fig. 2. The variety of the dynamics can be explained by the instability of sedimentation of a suspension of aggregating particles

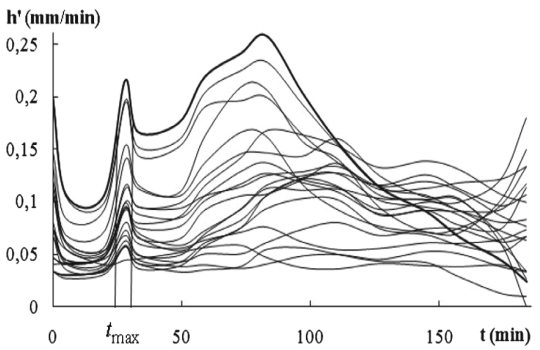

Fig. 2. Measured h′(t) curves and t_{max} location for 20 native blood samples of the same patient.

[24]. Anyway, for all the curves t_{max} values are located in quite narrow limits providing a high exactness in diagnosis of the drug allergy from the ESR tests in the microtubes.

3 Mathematical Problem Formulation

The mixture model of the blood as a three-phase continuous media composed of the free BP (phase 1), RBC aggregates (phase 2) and BP captured inside the aggregates (phase 3) includes the mass and momentum balance equations, and aggregate kinetics equations [27, 28]

$$\begin{aligned} &\frac{\partial \rho^{\alpha}}{\partial \mathrm{t}} + \mathrm{div}(\rho^{\alpha}\vec{\mathrm{v}}^{\alpha}) = \theta^{\alpha}, \\ &\rho^{\alpha}\frac{\mathrm{d}\vec{\mathrm{v}}^{\alpha}}{\mathrm{dt}} = -\mathrm{div}(\hat{\mathrm{P}}^{\alpha}) + \rho^{\alpha}\vec{\mathrm{f}}^{\alpha} + \vec{\mathrm{R}}^{\alpha}, \\ &\frac{\partial \mathrm{N}}{\partial \mathrm{t}} + \mathrm{div}(\mathrm{N}\vec{\mathrm{v}}^{2}) = \Gamma, \end{aligned} \tag{11}$$

where $\alpha = 1, 2, 3$ is the phase number, ρ^{α} are the densities of the phases, θ^{α} and $\vec{\mathrm{R}}^{\alpha}$ are the mass and momentum exchange due to the aggregation and BP capture, $\hat{\mathrm{P}}^{\alpha}$ are the stress tensors, $\vec{\mathrm{f}}^{\alpha}$ are the external forces, Γ is the RBC aggregation rate. In this model $\theta^2 = 0$ and θ^3 is the rate of BP capture during the aggregation.

According to the mixture theory

$$\rho^1 = (1 - \mathrm{H})\rho_{\mathrm{f}}, \quad \rho^2 = \mathrm{C}\rho_{\mathrm{s}}, \quad \rho^3 = (\mathrm{H} - \mathrm{C})\rho_{\mathrm{f}}, \tag{12}$$

where ρ_s, ρ_f are physical densities of RBC and BP.

Since the tube is thin ($d << L$), the radial and azimuthal motion can be neglected in comparison with vertical sedimentation and (11) can be written in 1d form.

Then substitution of (12) into the first Eq. (11) gives:

$$\begin{aligned} &\frac{\partial(1 - \mathrm{H})}{\partial \mathrm{t}} + \frac{\partial(1 - \mathrm{H})\mathrm{v}^1}{\partial \mathrm{x}} = -\theta; \\ &\frac{\partial \mathrm{C}}{\partial \mathrm{t}} + \frac{\partial \mathrm{C}\mathrm{v}^2}{\partial \mathrm{x}} = 0; \\ &\frac{\partial(\mathrm{H} - \mathrm{C})}{\partial \mathrm{t}} + \frac{\partial(\mathrm{H} - \mathrm{C})\mathrm{v}^3}{\partial \mathrm{x}} = \theta, \end{aligned} \tag{13}$$

where v^2 are vertical components of velocity vectors, $\theta = \theta^3/\rho_{\mathrm{f}}$.

Summation of (13) gives the incompressibility condition for the mixture

$$\frac{\partial}{\partial \mathrm{x}}\left[(1 - \mathrm{H})\mathrm{v}^1 + \mathrm{C}\mathrm{v}^2 + (\mathrm{H} - \mathrm{C})\mathrm{v}^3\right] = 0. \tag{14}$$

From the impermeability condition at the bottom of the tube

$$(1-\mathrm{H})\mathrm{v}^1+\mathrm{C}\mathrm{v}^2+(\mathrm{H}-\mathrm{C})\mathrm{v}^3=0 \tag{15}$$

and now from (14) one can obtain that (15) is valid at any cross section of the tube.

According to the thermodynamic model of 3-phase thixotropic fluid [27, 28]

$$\begin{aligned}
&\mathrm{P}^1_{\mathrm{lk}}=\left[\left(\mathrm{p}+\mathrm{p}^1_{\mathrm{H}}\right)(1-\mathrm{H})-\mu_1\mathrm{e}^1_{\mathrm{ii}}\right]\delta_{\mathrm{lk}}-2\mu_2\mathrm{e}^1_{\mathrm{lk}},\\
&\mathrm{P}^2_{\mathrm{lk}}=\left[\left(\mathrm{p}-\mathrm{p}^1_{\mathrm{s}}-\mathrm{p}^2_{\mathrm{s}}-\mathrm{p}^3_{\mathrm{s}}-\mathrm{p}^3_{\mathrm{H}}\right)\mathrm{C}-\mu_3\left(\mathrm{e}^2_{\mathrm{ii}}-\omega_{\mathrm{ii}}\right)\right]\delta_{\mathrm{lk}}-2\mu_4(\mathrm{e}_{\mathrm{lk}}-\omega_{\mathrm{lk}}),\\
&\mathrm{P}^2_{\mathrm{lk}}+\sigma_{\mathrm{lk}}=\left[\left(\mathrm{p}-\mathrm{p}^1_{\mathrm{s}}-\mathrm{p}^2_{\mathrm{s}}-\mathrm{p}^3_{\mathrm{s}}-\mathrm{p}^3_{\mathrm{H}}\right)\mathrm{C}-\mu_5\omega_{\mathrm{ii}}\right]\delta_{\mathrm{lk}}-2\mu_6\omega_{\mathrm{lk}},\\
&\mathrm{P}^3_{\mathrm{lk}}=\left[\left(\mathrm{p}-\mathrm{p}^2_{\mathrm{H}}-\mathrm{p}^3_{\mathrm{H}}\right)(\mathrm{H}-\mathrm{C})-\mu_7\mathrm{e}^3_{\mathrm{ii}}\right]\delta_{\mathrm{lk}}-2\mu_8\mathrm{e}^3_{\mathrm{lk}},\\
&\mathrm{R}^1_{\mathrm{l}}=\mathrm{F}\left(\mathrm{v}^2_{\mathrm{l}}-\mathrm{v}^1_{\mathrm{l}}\right)-\mathrm{p}\frac{\partial\mathrm{H}}{\partial\mathrm{x}_{\mathrm{l}}}+\mathrm{p}^1_{\mathrm{s}}\frac{\partial\mathrm{C}}{\partial\mathrm{x}_{\mathrm{l}}},\\
&\mathrm{R}^3_{\mathrm{l}}=\mathrm{D}\left(\mathrm{v}^2_{\mathrm{l}}-\mathrm{v}^3_{\mathrm{l}}\right)+\left(\mathrm{p}-\mathrm{p}^2_{\mathrm{H}}\right)\frac{\partial(\mathrm{H}-\mathrm{C})}{\partial\mathrm{x}_{\mathrm{l}}}+\left(\mathrm{p}^3_{\mathrm{s}}+\mathrm{p}^3_{\mathrm{H}}\right)\frac{\partial\mathrm{C}}{\partial\mathrm{x}_{\mathrm{l}}},
\end{aligned} \tag{16}$$

where μ_{j}, F, D are thermodynamic coefficients.

Substituting (16) into (14) and neglecting inertia, viscous stresses and assuming $\mathrm{p}^{\alpha}_{\mathrm{s}}=\mathrm{p}^{\alpha}_{\mathrm{H}}=0\quad(\alpha=1,3)$, $\varepsilon_{\mathrm{ll}}=0$ one can obtain the following momentum equations

$$\begin{aligned}
&-(1-\mathrm{H})\frac{\partial\mathrm{p}}{\partial\mathrm{x}}+(1-\mathrm{H})\rho_{\mathrm{f}}\mathrm{G}+\mathrm{F}\left(\mathrm{v}^2-\mathrm{v}^1\right)=0,\\
&-\mathrm{C}\frac{\partial\mathrm{p}}{\partial\mathrm{x}}+\frac{\partial\mathrm{p}^2_{\mathrm{s}}\mathrm{C}}{\partial\mathrm{x}}+\mathrm{p}^2_{\mathrm{H}}\frac{\partial(\mathrm{H}-\mathrm{C})}{\partial\mathrm{x}}-\mathrm{F}\left(\mathrm{v}^2-\mathrm{v}^1\right)-\mathrm{D}\left(\mathrm{v}^2-\mathrm{v}^3\right)+\mathrm{C}\rho_{\mathrm{s}}\mathrm{G}=0,\\
&-(\mathrm{H}-\mathrm{C})\frac{\partial\left(\mathrm{p}-\mathrm{p}^2_{\mathrm{H}}\right)}{\partial\mathrm{x}}+\mathrm{D}\left(\mathrm{v}^2-\mathrm{v}^3\right)+(\mathrm{H}-\mathrm{C})\rho_{\mathrm{f}}\mathrm{G},
\end{aligned} \tag{17}$$

where G(x) is external non-uniform force; in the gravity field G(x) = g.

From (15), (17) we have

$$\begin{aligned}
\mathrm{v}^1&=-\frac{\mathrm{H}(1-\mathrm{H})}{\mathrm{F}}\xi_1+\frac{(\mathrm{H}-\mathrm{C})^2}{\mathrm{D}}\xi_2,\\
\mathrm{v}^2&=\frac{(1-\mathrm{H})^2}{\mathrm{F}}\xi_1+\frac{(\mathrm{H}-\mathrm{C})^2}{\mathrm{D}}\xi_2,\\
\mathrm{v}^3&=\frac{(1-\mathrm{H})^2}{\mathrm{F}}\xi_1+\frac{(\mathrm{H}-\mathrm{C})(1-\mathrm{H}+\mathrm{C})}{\mathrm{D}}\xi_2,
\end{aligned} \tag{18}$$

where $\xi_1=\mathrm{C}(\rho_{\mathrm{s}}-\rho_{\mathrm{f}})\mathrm{G}+\frac{\partial}{\partial\mathrm{x}}\left[\mathrm{p}^2_{\mathrm{s}}\mathrm{C}+\mathrm{p}^2_{\mathrm{H}}(\mathrm{H}-\mathrm{C})\right]$, $\xi_2=\xi_1-\frac{\partial\mathrm{p}^2_{\mathrm{H}}}{\partial\mathrm{x}}$.

Now let us introduce an average volume of aggregates $w = C/N$ instead of N. Then from (18) one can derive the hyperbolic quasi-linear system of partial differential equations

$$\begin{aligned}
&\frac{\partial w}{\partial t} + v^2 \frac{\partial w}{\partial x} = -\frac{\Gamma w^2}{C},\\
&\frac{\partial H}{\partial t} + \gamma_{11} \frac{\partial H}{\partial x} + \gamma_{12} \frac{\partial C}{\partial x} + \gamma_{13} \frac{\partial w}{\partial x} = \theta,\\
&\frac{\partial C}{\partial t} + \gamma_{21} \frac{\partial H}{\partial x} + \gamma_{22} \frac{\partial C}{\partial x} + \gamma_{23} \frac{\partial w}{\partial x} = 0,
\end{aligned} \tag{19}$$

where

$$\begin{aligned}
&\gamma_{11} = v^1 - (1-H)\frac{\partial v^1}{\partial H}, \quad \gamma_{12} = -(1-H)\frac{\partial v^1}{\partial C}, \quad \gamma_{13} = -(1-H)\frac{\partial v^1}{\partial v},\\
&\gamma_{21} = C\frac{\partial v^2}{\partial H}, \quad \gamma_{22} = v^2 + C\frac{\partial v^2}{\partial C}, \quad \gamma_{23} = C\frac{\partial v^2}{\partial w},\\
&v^1 = \left[-\frac{H(1-H)}{F} + \frac{(H-C)^2}{D}\right] C(\rho_s - \rho_f)G, \quad v^2 = \left[\frac{(1-H)^2}{F} + \frac{(H-C)^2}{D}\right] C(\rho_s - \rho_f)G.
\end{aligned}$$

The system (19) must be solved at the following initial and boundary conditions

$$\begin{aligned}
&H(0,x) = H_0,\ C(0,x) = C_0,\ w(0,x) = w_0,\\
&v^1(t,L) = 0, \quad v^2(t,L) = 0,
\end{aligned} \tag{20}$$

where H_0, C_0, w_0 are initial values that are supposed to be constant in the sample.

Solution of (19) and (20) can be found by the method of characteristics. The system (19) has three families of characteristics

$$\begin{aligned}
&\left(\frac{dx}{dt}\right)_1 = v^2,\\
&\left(\frac{dx}{dt}\right)_{2,3} = \frac{\gamma_{11} + \gamma_{22} \pm \sqrt{(\gamma_{11} - \gamma_{22})^2 + 4\gamma_{12}\gamma_{21}}}{2}
\end{aligned} \tag{21}$$

with corresponding conditions

$$\begin{aligned}
&\frac{dw}{dt} = -\frac{\Gamma v^2}{C},\\
&\left[\left(\frac{dx}{dt}\right)_{2,3} - \gamma_{22}\right]\left(\frac{dH}{dt} - \theta\right) + \gamma_{12}\frac{dC}{dt} = 0\ .
\end{aligned} \tag{22}$$

Let us introduce the following velocities of the solid and fluid phases

$$\begin{aligned} \mathrm{v_s} &= (1-\mathrm{H})^2\mathrm{C}(\rho_\mathrm{s}-\rho_\mathrm{f})\mathrm{G}/\mathrm{F}, \\ \mathrm{v_f} &= (\mathrm{H}-\mathrm{C})^2\mathrm{C}(\rho_\mathrm{s}-\rho_\mathrm{f})\mathrm{G}/\mathrm{D}, \end{aligned} \tag{23}$$

then $\mathrm{v}^1 = -\mathrm{H}\mathrm{v_s}/(1-\mathrm{H}) + \mathrm{v_f}, \quad \mathrm{v}^2 = \mathrm{v_s} + \mathrm{v_f}$ and the expressions for the coefficients in (19) will be

$$\begin{aligned} &\gamma_{11} = \mathrm{v_s} + \mathrm{v_f} + \mathrm{H}\frac{\partial \mathrm{v_s}}{\partial \mathrm{H}} - (1-\mathrm{H})\frac{\partial \mathrm{v_f}}{\partial \mathrm{H}}, \quad \gamma_{22} = \mathrm{v_s} + \mathrm{v_f} + \mathrm{C}\frac{\partial \mathrm{v_s}}{\partial \mathrm{C}} + \mathrm{C}\frac{\partial \mathrm{v_f}}{\partial \mathrm{C}}, \\ &\gamma_{12} = \mathrm{H}\frac{\partial \mathrm{v_s}}{\partial \mathrm{C}} - (1-\mathrm{H})\frac{\partial \mathrm{v_f}}{\partial \mathrm{C}}, \quad \gamma_{21} = \mathrm{C}\frac{\partial \mathrm{v_s}}{\partial \mathrm{H}} + \mathrm{C}\frac{\partial \mathrm{v_f}}{\partial \mathrm{H}}\ . \end{aligned} \tag{24}$$

Substitution of (23) into (21) and (22) gives

$$\begin{aligned} &\left(\frac{\mathrm{dx}}{\mathrm{dt}}\right)_1 = \mathrm{v_s} + \mathrm{v_f}, \\ &\left(\frac{\mathrm{dx}}{\mathrm{dt}}\right)_{2,3} = \mathrm{v_s} + \mathrm{v_f} + \frac{1}{2}\mathrm{A}\left(1 \pm \sqrt{1-\mathrm{B}/\mathrm{A}^2}\right), \end{aligned} \tag{25}$$

$$\begin{aligned} &\frac{\mathrm{dw}}{\mathrm{dt}} = -\frac{\Gamma \mathrm{v}^2}{\mathrm{C}}, \\ &\frac{1}{2}\left[\mathrm{A}_1\left(1+\sqrt{1-\mathrm{B}/\mathrm{A}^2}\right) - \mathrm{A}_2\left(1-\sqrt{1-\mathrm{B}/\mathrm{A}^2}\right)\right]\left(\frac{\mathrm{dH}}{\mathrm{dt}} - \theta\right) + \gamma_{12}\frac{\mathrm{dC}}{\mathrm{dt}} = 0, \\ &\frac{1}{2}\left[\mathrm{A}_1\left(1-\sqrt{1-\mathrm{B}/\mathrm{A}^2}\right) - \mathrm{A}_2\left(1+\sqrt{1-\mathrm{B}/\mathrm{A}^2}\right)\right]\left(\frac{\mathrm{dH}}{\mathrm{dt}} - \theta\right) + \gamma_{12}\frac{\mathrm{dC}}{\mathrm{dt}} = 0, \end{aligned} \tag{26}$$

where

$$\begin{aligned} &\mathrm{A}_1 = \mathrm{H}\frac{\partial \mathrm{v_s}}{\partial \mathrm{H}} - (1-\mathrm{H})\frac{\partial \mathrm{v_f}}{\partial \mathrm{H}}, \quad \mathrm{A}_2 = \mathrm{C}\frac{\partial \mathrm{v_s}}{\partial \mathrm{C}} + \mathrm{C}\frac{\partial \mathrm{v_f}}{\partial \mathrm{C}}, \quad \mathrm{A} = \mathrm{A}_1 + \mathrm{A}_2, \\ &\mathrm{B} = 4\mathrm{C}\left(\frac{\partial \mathrm{v_s}}{\partial \mathrm{H}}\frac{\partial \mathrm{v_f}}{\partial \mathrm{C}} - \frac{\partial \mathrm{v_s}}{\partial \mathrm{C}}\frac{\partial \mathrm{v_f}}{\partial \mathrm{H}}\right). \end{aligned}$$

Based on the dimension analysis, one may have

$$\mathrm{F} = \mu \mathrm{w}^{-2/3}\phi_1(\mathrm{H},\mathrm{C},\chi_\mathrm{i}), \quad \mathrm{D} = \mu \mathrm{v}_0^{-2/3}\phi_2(\mathrm{H},\mathrm{C},\xi_\mathrm{i}), \tag{27}$$

where $\phi_1,\ \phi_2$ are dimensionless functions that can be derived from experiments in the form

$$\phi_1 = \alpha \mathrm{H}(1-\mathrm{H})^{-\eta_1},\ \phi_2 = \beta \mathrm{C}(1-\mathrm{C}/\mathrm{H})^{-\eta_2}$$

where $\alpha,\ \beta,\ \eta_1,\ \eta_2$ are positive constants.

Finally, we have from (27)

$$\mathrm{F} = \alpha\mu\mathrm{H}(1-\mathrm{H})^{-\eta_1}(\mathrm{H}/\mathrm{C})^{2/3}\mathrm{w}^{-2/3},\ \mathrm{D} = \beta\mu\mathrm{C}(1-\mathrm{C}/\mathrm{H})^{-\eta_2}\mathrm{w}_0^{-2/3}. \tag{28}$$

Substitution of (28) into (18) gives the expressions for velocities
$\mathrm{v_s} = \frac{(1-\mathrm{H})^{2+\eta_1}(\mathrm{C}/\mathrm{H})^{1/3}\mathrm{w}^{2/3}(\rho_s-\rho_f)\mathrm{G}}{\alpha\mu}$, $\mathrm{v_f} = \frac{(1-\mathrm{H})^2(1-\mathrm{C}/\mathrm{H})^{\eta_2}\mathrm{w}_0^{2/3}(\rho_s-\rho_f)\mathrm{G}}{\beta\mu}$.
Now one can obtain

$$\begin{aligned}
\frac{\partial \mathrm{v_s}}{\partial \mathrm{H}} &= -\frac{1+(3\eta_1+5)\mathrm{H}}{3\mathrm{H}(1-\mathrm{H})}\mathrm{v_s}, \quad \frac{\partial \mathrm{u_s}}{\partial \mathrm{C}} = \frac{1}{3\mathrm{C}}\mathrm{v_s} \\
\frac{\partial \mathrm{v_f}}{\partial \mathrm{H}} &= \frac{2+\eta_2\mathrm{C}/\mathrm{H}}{\mathrm{H}-\mathrm{C}}\mathrm{v_f}, \quad \frac{\partial \mathrm{u_f}}{\partial \mathrm{C}} = -\frac{2+\eta_2}{\mathrm{H}-\mathrm{C}}\mathrm{v_f}
\end{aligned} \tag{29}$$

Accounting for (29), the coefficients $\mathrm{A}_1,\ \mathrm{A}_2,\ \mathrm{A},\ \mathrm{B},\ \gamma_{12}$ in (26) will have the form

$$\begin{aligned}
\mathrm{A}_1 &= -\frac{1+(3\eta_1+5)\mathrm{H}}{3(1-\mathrm{H})}\mathrm{v_s} - \frac{(2+\eta_2\mathrm{C}/\mathrm{H})(1-\mathrm{H})}{\mathrm{H}-\mathrm{C}}\mathrm{v_f} \\
\mathrm{A}_2 &= \frac{1}{3}\mathrm{u_s} - \frac{(2+\eta_2)\mathrm{C}}{\mathrm{H}-\mathrm{C}}\mathrm{u_f} \\
\mathrm{A} &= -\frac{(\eta_1+2)\mathrm{H}}{1-\mathrm{H}}\mathrm{v_s} - \left[\frac{2(1-\mathrm{H}+\mathrm{C})+\eta_2\mathrm{C}/\mathrm{H}}{\mathrm{H}-\mathrm{C}}\right]\mathrm{v_f} \\
\mathrm{B} &= \frac{4\mathrm{C}}{\mathrm{H}-\mathrm{C}}\left[\frac{1+(3\eta_1+5)H}{3\mathrm{H}(1-\mathrm{H})}(2+\eta_2) - \frac{(2+\eta_2\mathrm{C}/\mathrm{H})}{3\mathrm{C}}\right]\mathrm{v_s}\mathrm{v_f} \\
\gamma_{12} &= \frac{\mathrm{H}}{3\mathrm{C}}\mathrm{v_s} + \frac{(1-\mathrm{H})(2+\eta_2)}{\mathrm{H}-\mathrm{C}}\mathrm{v_f}\ .
\end{aligned} \tag{30}$$

Now numerical computations on (25) and (26) can be carried out. At the beginning of the RBC sedimentation $\mathrm{v_f} << \mathrm{v_s}$ because $(\mathrm{H}-\mathrm{C})/(1-\mathrm{H}) << 1$. Then one can neglect the terms $\sim \mathrm{v_f}/\mathrm{v_s}$ and rewrite (25) and (26) in a simple form

$$\left(\frac{\mathrm{dx}}{\mathrm{dt}}\right)_1 = \mathrm{v_s}, \quad \left(\frac{\mathrm{dx}}{\mathrm{dt}}\right)_2 = -\left[\frac{(\eta_2+2)\mathrm{H}}{1-\mathrm{H}} - 1\right]\mathrm{v_s}, \quad \left(\frac{\mathrm{dx}}{\mathrm{dt}}\right)_3 = \mathrm{v_s}, \tag{31}$$

$$\frac{\mathrm{dw}}{\mathrm{dt}} = -\frac{\Gamma\mathrm{v}^2}{\mathrm{C}}, \quad \left[-\frac{1+(3\eta_1+5)\mathrm{H}}{3(1-\mathrm{H})}\right]\left(\frac{\mathrm{dH}}{\mathrm{dt}} - \theta\right) + \frac{\mathrm{H}}{3\mathrm{C}}\frac{\mathrm{dC}}{\mathrm{dt}} = 0, \quad \frac{\mathrm{dH}}{\mathrm{dt}} - \frac{\mathrm{H}}{\mathrm{C}}\frac{\mathrm{dC}}{\mathrm{dt}} = \theta. \tag{32}$$

At the end of the test the RBC are no longer in a free fall and $\mathrm{u_s} << \mathrm{u_f}$ [32]. In this case one can neglect in (26) the terms $\sim \mathrm{u_s}/\mathrm{u_f}$ and assume $\mathrm{H} \sim 1$, and have (26) and (27) as the following

$$\left(\frac{\mathrm{dx}}{\mathrm{dt}}\right)_1 = \mathrm{v_f}, \quad \left(\frac{\mathrm{dx}}{\mathrm{dt}}\right)_2 = -\left[\frac{2(1-\mathrm{H}+\mathrm{C})+\eta_2\mathrm{C}/\mathrm{H}}{\mathrm{H}-\mathrm{C}}\right]\mathrm{v_f}, \quad \left(\frac{\mathrm{dx}}{\mathrm{dt}}\right)_3 = \mathrm{v_f}, \tag{33}$$

$$\frac{dw}{dt} = -\frac{\Gamma v^2}{C}, \quad -\left(\frac{dH}{dt} - \theta\right) + \left(\frac{2+\eta_2}{2+\eta_2 C/H}\right)\frac{dC}{dt} = 0,$$
$$C\left(\frac{dH}{dt} - \theta\right) + (1-H)\frac{dC}{dt} = 0. \tag{34}$$

As one can see from (26), the first characteristics is always positive ($(dx/dt)_1 > 0$), third one is negative ($(dx/dt)_3 < 0$), while the second one $\left(\frac{dx}{dt}\right)_3 > 0$ when $H \in \left(0, (\eta_1+3)^{-3}\right)$ and $\left(\frac{dx}{dt}\right)_3 < 0$ when $H \in \left((\eta_1+3)^{-3}, 1\right)$.

Numerical computations on (26) and (27) have been carried out using the model parameters for the blood samples examined in the experiments (see Chap. 2)

$$H_0 = 30 \div 50\%,\ \mu_f = (1.1 \div 1.7)\cdot 10^{-3}\,\mathrm{Pa\cdot s},\ G = g,$$
$$\rho_f = 1030 \div 1080\,\mathrm{kg/m^3},\ \rho_s = 1050 \div 1150\,\mathrm{kg/m^3}.$$

4 Results and Discussions

When the BP capture inside the aggregates can be neglected, from (26) and (27) one can obtain two characteristics; the positive one started from the top of the tube x = 0 and the negative one started from the bottom x = L (Fig. 3). For simplicity, the vertical axes is located down along the gravity field (Fig. 3a) and the regions 1, 2, 3 (Fig. 3b) correspond to the zones of clear BP, settling aggregates and compact RBC network [32]. The two characteristics meet at $t = t_{max}$ when the ESR reach its maximal value (Fig. 3). At $t > t_{max}$ the compact RBC network influence the settling aggregates that reducing the ESR.

Based on (25)–(27), the following expression for the time t_{max} has been obtained

$$t_{max} = \frac{1}{kH_0}\left[\left(\frac{5kH_0 f(H_0)}{3[1-\gamma(H_0)](1-H_0)^2} + 1\right)^{0.6} - 1\right], \tag{35}$$

where $\gamma(H) = 1 + (H/v)/(\partial v/\partial H)$.

When the BP capture inside the aggregates is essential, three families of characteristics produce four regions by their cross sections (Fig. 4a, b). Depending whether the third characteristics is positive or negative, two different distributions can be seen. The first zone again corresponds to the clear BP region, while zone 2 is field with single RBC and small aggregates distributed in BP. Zone 3 corresponds to the aggregating RBCs and settling aggregates, while zone 4 is the compact zone composed by the resting aggregates with a small amount of BP. Depending on the model parameters the height h_2 of the zone 2 may be small ($h_2 << h_3$, Fig. 4a) or big ($h_2 >> h_3$, Fig. 4b) at the same values h_1, h_4. In the experiments both cases have been observed. The zone 2 has been present and semi-transparent pink or red colored region. Most likely, the zone

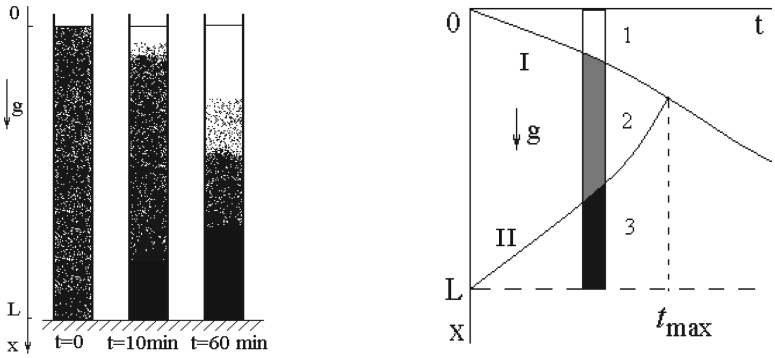

Fig. 3. Schematic representation of the sedimentation dynamics at different times (a) according to two families of characteristics (I, II) (b).

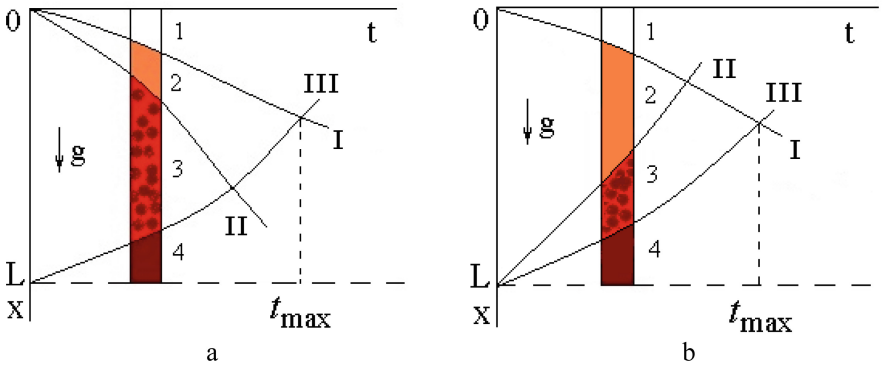

Fig. 4. Schematic representation of the sedimentation dynamics according to three characteristics (I, II, III) with positive (a) and negative (b) 2-nd characteristic.

2 correspond to the BP released at high vertical velocities from the aggregates due to instability and rapid compression of the RBC network in the zone 3 [32].

The software allowed numerical computations of the concentrations and velocities in each zone based on the method of characteristics has been developed. The mesh composed by three families of characteristics is depicted in Fig. 5. The convergence has been reached very fast starting with the division of the length $X \in [0, 1]$ into 20 segments. The location of the cross section point (t_{max}) is strongly determined by the model parameters.

Some numerical results are presented in Figs. 6 and 7a–c. Three types of sedimentation dynamics have been observed. At some combinations of the model parameters the ESR almost linear increases during the first 20–35 min of sedimentation and then sedimentation almost stopped (Figs. 6a and 7a). In other cases the ESR curves are S-shaped with initial slow ESR replaced by faster sedimentation, which is decelerated then till to the constant sedimentation velocity (Figs. 6c and 7c). When initial

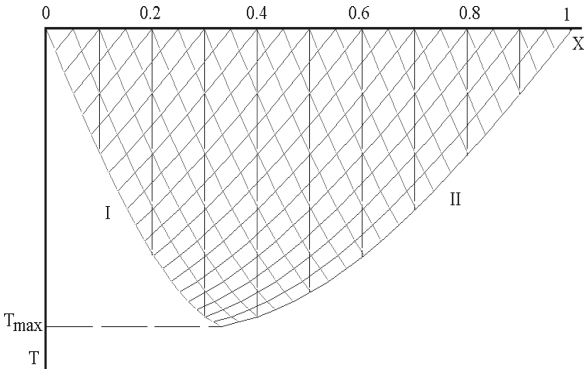

Fig. 5. Two families (I and II) of characteristics and determination of $t_{\max}$.

acceleration was non-linear but without typical S-shape, the ESR curves were classified as intermediate ones (Figs. 6b and 7b). The main factors influenced the initial acceleration of sedimentation were initial RBC concentration H_0, BP viscosity μ_f, and RBC aggregation rate k. At low $H_0 \leq 35\%$ slow linear increase $h_1(t)$ has been observed (Fig. 6a). The 60 min values of h_1 corresponded to healthy organisms at $k = 10^5 - 10^6$, while $k = 10^7 - 10^9$ were proper to the h_1 values corresponded to pneumonia, moderate inflammations, and some other diseases [2, 3]. At low initial concentrations and elevated BP viscosity or/and density the intermediate cases have been observed (Fig. 6b). In this case the same influence of the aggregation rate has been revealed. When $H_0 \geq 45\%$ and ρ_f, μ_f are increased, the typical S-shaped ESR curves have been computed. Those combinations of the rheological parameters correspond to unclear BP filled with reactive proteins [5, 6] that is proper to severe inflammations, and cancer [2, 3].

Based on the computation data, the values t_{max} have been computed from the differential curves $h'(t)$ and on (35). It was shown, the characteristic values of the RBC aggregation rate k measured on the control group, were in the range $k \in [1.2 \cdot 10^5, 2.9 \cdot 10^7]$, while in the patients with allergy $k \in [9.3 \cdot 10^8, 7.9 \cdot 10^9]$ [24]. Similar computations on the ESR curves measured on the patients with different types of cancer [32] revealed the values $k > 10^{10}$. Since cancer leads to significant variations of thickness and structure of RBC hydration shells [20], the observed extremely elevated ESR values are connected with RBC surface changes by cancer disease, their interconnected electrical and mechanical properties. It was show, the RBC surface properties, structure and thickness of their hydration shells restore after successful X-ray and/or chemotherapy that is shown by their dielectric and temperature spectra [33]. Therefore, the ESR curves can be also used for control of the outcomes of the prescribed treatment and prognosis of disease. This important clinical application must be first tested on several groups of patients and healthy donors that will be done in out next study.

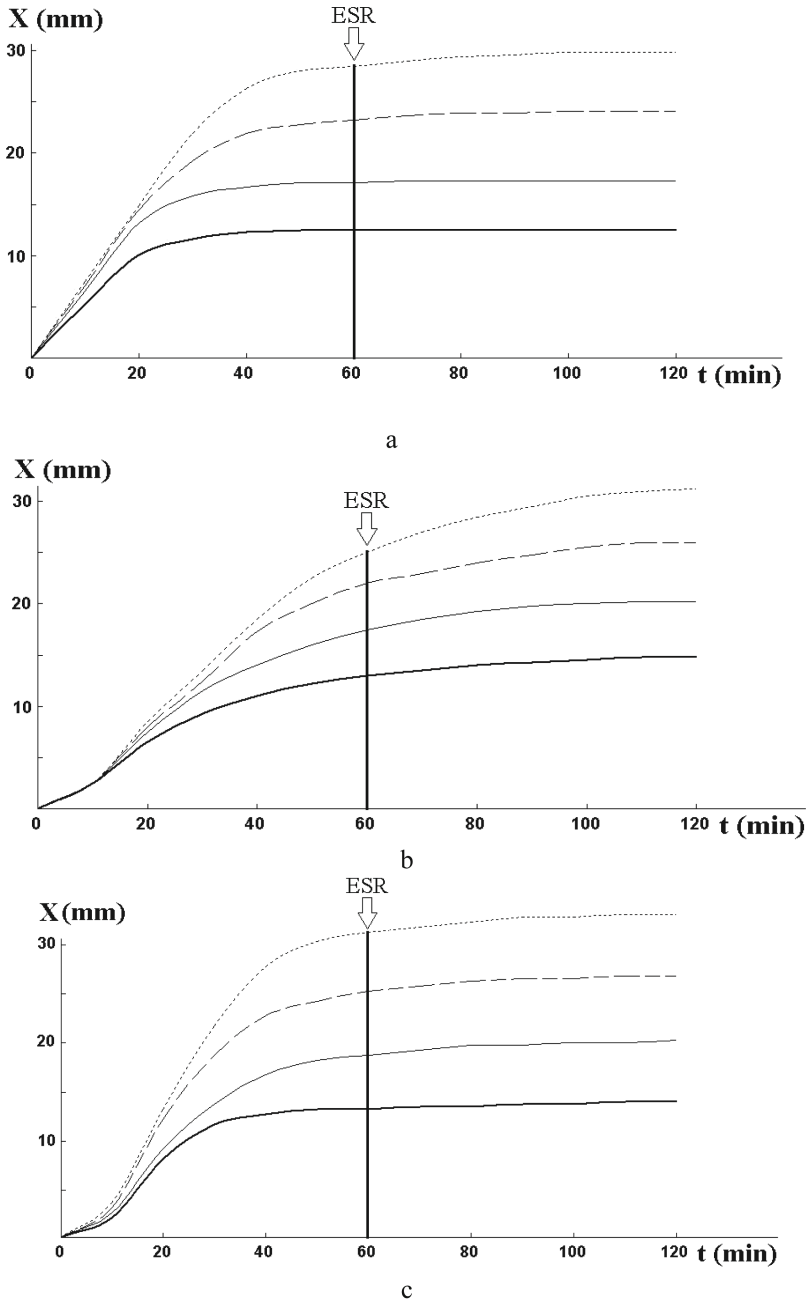

Fig. 6. ESR curves X(t) at $H_0 = 30\%, \mu = 5 \cdot 10^{-3} Pa \cdot s$ (a), $H_0 = 40\%, \mu = 4 \cdot 10^{-3} Pa \cdot s$ (b), $H_0 = 48\%, \mu = 3 \cdot 10^{-3} Pa \cdot s$ (c), at k = 10^5 (thick line), k = 10^6 (thin line), k = 10^7 (dashed line), k = 10^8 (dotted line).

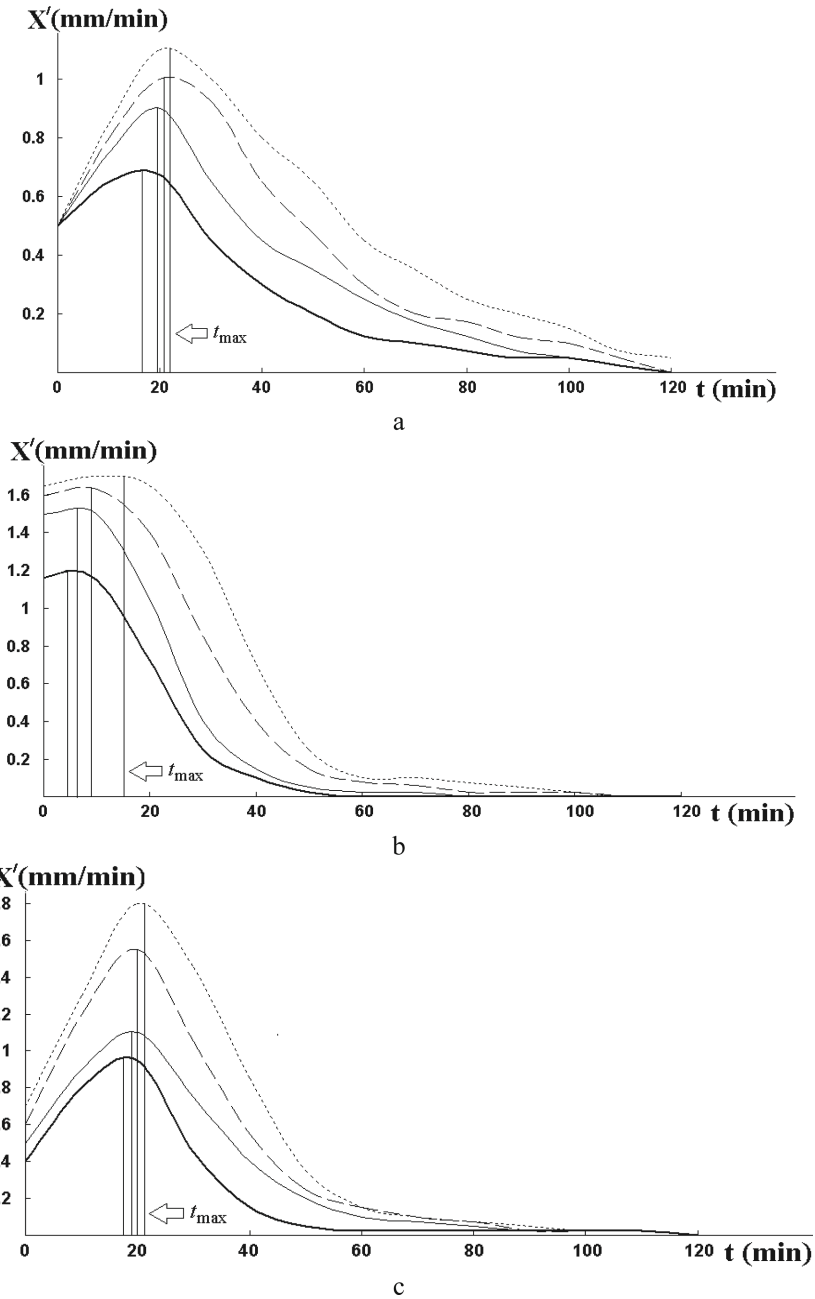

Fig. 7. Differential ESR curves X′(t) at $H_0 = 30\%, \mu = 5 \cdot 10^{-3} Pa \cdot s$ (a), $H_0 = 40\%, \mu = 4 \cdot 10^{-3} Pa \cdot s$ (b), $H_0 = 48\%, \mu = 3 \cdot 10^{-3} Pa \cdot s$ (c), at $k = 10^5$ (thick line), $k = 10^6$ (thin line), $k = 10^7$ (dashed line), $k = 10^8$ (dotted line).

5 Conclusions

The ESR is a very simple diagnostic test, which is widely used for non-specific diagnostics of the state of an organism, possible inflammations, ageing and mental disorders and some specific diseases. The ERS curves X(t) measured by computer assisted equipment carry more information on aggregation dynamics and specific interactions between RBC, BP proteins, products of the soft-tissue decay, apoptosis or new growth. The differential $h'(t)$ curves reveal stable time intervals t_{max} when $h'(t) \rightarrow$ max. A modification of the ESR test when a small portion of potential allergen (pollen, drug or food allergens) is added to the stabilized native blood is very helpful in revealing different food and drug allergy. It gives a new tool for fast and cheap quantitative estimation of the allergy and personal compatibility with prescribed medicine. An addition of the allergen can lead either to acceleration or to deceleration of the ESR in comparison with the control probe. Due to instability of the sedimentation process when occasional formation of a large aggregate at the top of the sedimentation tube could fall down faster and accelerate the process, the study of several (3–5) probes with the same allergen could be recommended. The decision can be made on the averaged value of t_{max} and averaged ESR curves.

References

1. Fung, Y.C.: Biomechanics. Circulation. Springer, New York (1997). https://doi.org/10.1007/978-1-4757-2696-1
2. Baskurt, O.K., Hardeman, M.R., Rampling, M.W.: Handbook of Hemorheology and Hemodynamics. IOS Press, Amsterdam (2007)
3. Olshaker, J.S., Jerrard, D.A.: The erythrocyte sedimentation rate. J. Emergency Med. **15**(6), 869–874 (1997)
4. Calderon, A.J., Wener, M.H.: Erythrocyte sedimentation rate and C-reactive protein. Hosp. Med. Clin. **193**, 313–337 (2012)
5. Litao, M.K., Kamat, D.: Erythrocyte sedimentation rate and C-reactive protein: how best to use them in clinical practice. Pediatr. Ann. **43**(10), 417–420 (2014)
6. Kainth, M.K., Gigliotti, F.: Simultaneous testing of erythrocyte sedimentation rate and C-reactive protein: increased expenditure without demonstrable benefit. J. Pediatr. **165**(3), 625–627 (2014)
7. Grzybowski, A., Sak, J.: Edmund Biernacki (1866–1911): discoverer of the erythrocyte sedimentation rate. On the 100th anniversary of his death. Clin. Dermatol. **29**(6), 697–703 (2011)
8. Daniels, L.M., Tosh, P.K., Fiala, J.A., et al.: Extremely elevated erythrocyte sedimentation rates: associations with patients' diagnoses, demographic characteristics, and comorbidities. Mayo Clinic Proc. **92**(11), 1636–1643 (2017)
9. Cengiz, O.K., Esmen, S.E., Varli, M., et al.: Markedly elevated erythrocyte sedimentation rate in older adults. How significant clinically? Eur. Geriatr. Med. **4**(1), 28–31 (2013)
10. Shteinshnaider, M., Almoznino-Sarafian, D., Tzur, I., et al.: Shortened erythrocyte sedimentation rate evaluation is applicable to hospitalised patients. Europ. J. Internal Med. **21**(3), 226–229 (2010)

11. Karlsson, H., Ahlborg, B., Dalman, Ch., Hemmingsson, T.: Association between erythrocyte sedimentation rate and IQ in Swedish males aged 18–20. Brain Behav. Immun. **24**(6), 868–873 (2010)
12. van den Broek, N.R., Letsky, E.A: Pregnancy and the erythrocyte sedimentation rate. Br. J. Obstet. Gynaecol. **108**(11), 1164–1167 (2001)
13. Choi, J.W., Pai, S.H.: Influences of hypercholesterolemia on red cell indices and erythrocyte sedimentation rate in elderly persons. Clin. Chim. Acta **341**(1–2), 117–121 (2004)
14. Ingelsson, E., Årnlöv, J., Sundström, J., Lind, L.: Inflammation, as measured by the erythrocyte sedimentation rate, is an independent predictor for the development of heart failure. J. Amer. Coll. Cardiol. **45**(11), 1802–1806 (2005)
15. Rabjohn, L., Roberts, K., Troiano, M., Schoenhaus, H.: Diagnostic and prognostic value of erythrocyte sedimentation rate in contiguous osteomyelitis of the foot and ankle. J. Foot Ankle Surg. **46**(4), 230–237 (2007)
16. Glaser, R.: Biophysics: An Introduction. Springer, Berlin (2012)
17. Alison, J., Sheppard, R.: Dielectric properties of human blood at microwave frequencies. Phys. Med. Biol. **38**, 971–978 (1993)
18. Jaspard, F., Nadi, M., Rouane, A.: Dielectric properties of blood: an investigation of haematocrit dependence. Physiol. Meas. **24**, 137–147 (2003)
19. Lisin, R., Ginzburg, B.Z., Schlesinger, M., Feldman, Y.: Time domain dielectric spectroscopy study of human cells: I. Erythrocytes and ghosts. Biochim. Biophys. Acta **1280**(1), 34–40 (1996)
20. Batyuk, L.: Influence of cancer disease on dielectric characteristics of structural-functional state of erythrocyte membranes. ScienceRise Med. Sci. **7**(12), 11–17 (2015)
21. Bertoluzzo, S.M., Bollini, A., Rasia, M., Raynal, A.: Kinetic model for erythrocyte aggregation. Blood Cells Mol. Dis. **25**(2), 339–349 (1999)
22. Bell, G.I.: Models for the specific adhesion of cells to cells. Science **200**(1088), 618–627 (1978)
23. Chesnutt, J.K.W., Marshall, J.S.: Blood cell transport and aggregation using discrete ellipsoidal particles. Comput. Fluids **38**(6), 1782–1794 (2009)
24. Kizilova, N., Cherevko, V.: Mathematical modeling of particle aggregation and sedimentation in concentrated suspensions. In: Korzynski, M., Czwanka, J. (eds.) Mechanika w Medycynie, vol. 12, pp. 43–52. Rzeszow Univ. Press (2014)
25. Provata, A., Trohidou, K.N.: Spatial distribution and fractal properties of aggregating magnetic and non-magnetic particles. Fractals **6**(2), 219–230 (1998)
26. Neu, B., Miesleman, H.J.: Depletion-mediated red blood cell aggregation in polymer solutions. Biophys. J. **83**(5), 2482–2490 (2002)
27. Regirer, S.A.: On continual models of suspensions. Appl. Math. Mech. **42**(4), 679–688 (1978)
28. Regirer, S.A., Shadrina, N.H.: On models of tixotropic liquids. Appl. Math. Mech. **42**(5), 856–865 (1978)
29. Regirer, S.A.: Lectures on Biological Mechanics. Moscow University Press, Moscow (1980)
30. Kizilova, N.: Aggregation in magnetic field. In: Contemporary Problems of Biomechanics, vol. 9, pp. 118–135. Moscow University Press, Moscow (1994)
31. Chesnutt, J.K.W., Marshall, J.S.: Blood cell transport and aggregation using discrete ellipsoidal particles. Comput. Fluids **38**(5), 1782–1794 (2009)
32. Pribush, A., Meyerstein, D., Meyerstein, N.: The mechanism of erythrocyte sedimentation. Part 2: The global collapse of settling erythrocyte network. Colloids Surf. B Biointerfaces **75** (1), 224–229 (2010)
33. Batyuk, L., Kizilova, N.: Thermodynamic approach to dielectric parameters of human blood: application to early medical diagnostics of tumors. In: 14th Joint European Thermodynamics Conference, Book of Abstracts, Budapest (2017)